Surface & Coatings Technology 504 (2025) 132061

Contents lists available at ScienceDirect

Surface & Coatings Technology

journal homepage: www.elsevier.com/locate/surfcoat

Advancing aeronautical surface texturing: Through-mask electrochemical micromachining of aluminum AA2024-T3 for drag reduction applications

Andrea Cristoforetti [b,*], Matteo Gamba [a], Andrea Brenna [a], Marco Ormellese [a], Michele Fedel [b]

[a] Department of Chemistry, Materials and Chemical Engineering "Giulio Natta", Politecnico di Milano, Via Mancinelli 7, 20131 Milan, Italy
[b] Department of Industrial Engineering, University of Trento, 38123 Trento, TN, Italy

ARTICLE INFO

Keywords:
Shark skin
Through-mask electrochemical micromachining
Drag reduction
Surface texturing
Electrochemical etching
Aluminum

ABSTRACT

Surface texturing is crucial in various fields including electronics, energy, optics, and biology. Inspired by sharkskin microstructures, riblet surfaces have been extensively studied for their drag-reducing properties, particularly in aeronautical applications. Existing solutions for surface texturing based on shaped polymeric foils, however, often face wear issues and require frequent maintenance. To overcome these challenges, through-mask electrochemical micromachining (TMEMM) offers a promising approach. This study investigates TMEMM's applicability for mimicking sharkskin riblets on aluminum alloys, focusing on AA2024-T3. Ink-jet technology is introduced for mask deposition, enabling precise coverage and reducing waste. The masked samples undergo anodic polarization, with continuous and pulsed currents compared. The etching electrolyte composition is discussed and the addition of complexing agents is evaluated. Experimental results shed light on optimizing TMEMM parameters for fabricating complex structures on AA2024-T3, offering insights for riblets-base drag reduction in aeronautical applications. The crucial aspect for shaping the pointed geometry of the riblets lies in effectively combining etching parameters to ensure balanced removal rates across both depth and lateral directions.

1. Introduction

1.1. Sharkskin bio-mimic for fluids drag reduction

Surface texturing plays a pivotal role in various advanced domains including electronics, energy, optics, information technology, tribology, biology, and biomimetics [1,2]. Notably, research inspired by the sharkskin (Fig. 1a), particularly the micro-scaled dermal denticles or riblets found on the skin of the mako shark, has significantly contributed to fluid dynamics studies [3,4]. Riblets textured surfaces, comprising grooves aligned with the flow direction, have been extensively investigated for their ability to prevent vortex formation or divert them away from the surface [5,6], thereby reducing fluid drag, especially in aeronautical applications starting from the initial study by Walsh et al. in 1979 [7]. Reducing energy consumption, enhancing cost-effectiveness, and improving environmental efficiency are all direct and desirable outcomes of successful flow control. In their simplest configuration, riblets are small, two-dimensional protrusions aligned with the flow direction, creating anisotropic wall roughness. In essence, riblets are effective because their particular geometry restricts spanwise near-wall flow more than the streamwise flow. A schematic of the riblet geometry, with a triangular cross-sectional shape, is shown in Fig. 2. Experiments by Bechert et al. [8], along with theoretical and numerical studies by Luchini et al. [9], have elucidated the drag reduction mechanism. This mechanism can be interpreted as an apparent shift in the velocity profile within the turbulent region of the boundary layer. It has been demonstrated that when the spanwise peak-to-peak spacing between riblet crests is sufficiently small (i.e., in the so-called viscous regime), the drag reduction rate is linearly dependent on a quantity called the protrusion height difference, Δh_p. This is defined as the difference between the longitudinal protrusion height and the transverse protrusion height, which correspond to the virtual origins of the longitudinal and transverse velocity profiles, respectively (Fig. 1b).

Although each protrusion height is measured from an arbitrarily defined reference point (such as the riblet tip), their difference is independent of the chosen reference, making Δh_p a well-defined and non-arbitrary quantity. When Δh_p is positive, the spanwise flow induced by the overlying turbulent streamwise vortices is impeded more than the

* Corresponding author.
E-mail addresses: andrea.cristoforetti@unitn.it (A. Cristoforetti), matteo.gamba@polimi.it (M. Gamba), andrea.brenna@polimi.it (A. Brenna), marco.ormellese@polimi.it (M. Ormellese), michele.fedel@unitn.it (M. Fedel).

https://doi.org/10.1016/j.surfcoat.2025.132061
Received 4 February 2025; Received in revised form 7 March 2025; Accepted 18 March 2025
Available online 19 March 2025

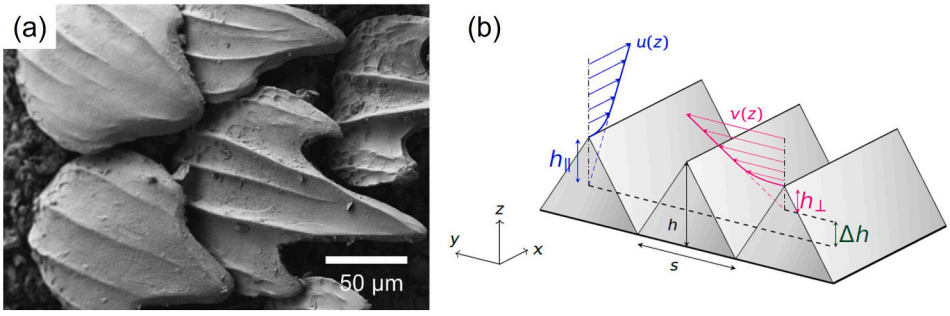

Fig. 1. Scanning electron micrographs of the typical riblet structure of shark skin. Adapted from [15] (a) and Sketch of the two protrusion heights (arbitrarily defined from the riblets tip) and the origin-independent protrusion heights difference $\Delta h_p = \Delta_\parallel - \Delta_\perp$ (b).

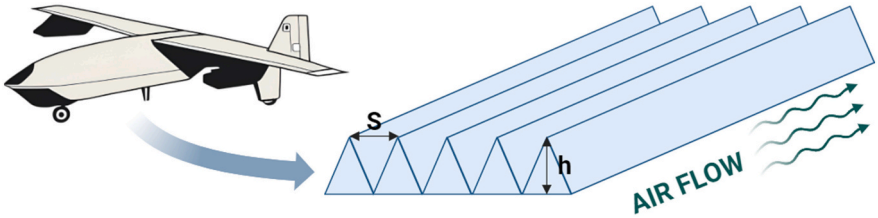

Fig. 2. Example of potential surface texturing concept on an aerial vehicle.

longitudinal flow. This results in a weakening of the turbulence-regeneration cycle near the wall, reduced turbulent activity, and ultimately a reduction in turbulent drag.

After riblets were proven effective, researchers focused on finding the optimal shape to enhance their performance. It has been determined that while the specific shape of the riblets' cross-section is not crucial, their dimensions are. The effectiveness of riblets is influenced more by their size than by their exact shape. Studies have shown that adjusting the spanwise width of the riblets can affect drag reduction, and there is a preferred range for this width that maximizes performance [10].

On the other hand, the sharpness of riblet tips is crucial for their drag-reduction performance. Rounded or worn tips significantly reduce their effectiveness. This is a major concern, especially in aeronautical applications where the riblets are very small and subject to wear from dust and debris during operations.

Besides the means of aerial transport field, these biomimetic surfaces also found applications in wind turbine components and marine vessels [11,12]. In applications that involve water as a working fluid, the issues related to bio-fouling are of paramount importance [13,14] as they limit the applicability of the riblet surfaces in this environment.

1.2. Texturing technology

To date, existing texturing solutions in the aeronautical field, such as polymeric adhesives with riblet structures or components produced through additive manufacturing [16], often show limited durability, as they suffer from severe mechanical wear, implying frequent maintenance and making them economically poorly competitive [3,17]. To address these challenges, alternative approaches for surface texturing could be explored. Previous studies have demonstrated the creation of microstructures such as micro-pillars and grooves directly on metal surfaces through techniques like laser ablation [18] and wire-cutting machining combined with chemical etching [19] to obtain super-hydrophobic surfaces, and electroplating for electronics cooling [20]. However, these methods may introduce surface imperfections or require precise and costly equipment. For example, laser machining causes the creation of casting layers, spatter, and micro-cracking in the vicinity of treated regions. This adversely affects the initial surface smoothness, requiring subsequent processing steps [21].

In this context, through-mask electrochemical micromachining (TMEMM) emerges as a promising low-damage and residual stress-free machining method capable of producing complex microstructures on metal substrates [22]. The process involves the use of a metal substrate as the anode in an electrochemical cell, causing it to dissolve in a controlled manner. By covering the substrate with an insulating mask, localized and selective material removal is induced. In this way, it is possible to produce different 3D textures on the surface depending on the masking pattern shielding it. However, existing techniques have primarily focused on producing grooves rather than micro-riblets [23,24], and the application of TMEMM on aluminum alloys, particularly the irksome AA2024, remains unexplored. This study aims to address this gap by employing TMEMM to mimic micro-riblets scales of the mako shark skin on aluminum for aeronautical application to improve its fluid-dynamic features by surface texturing.

This could be accomplished first by depositing a pattern of parallel lines of insulating material, typically polymer-based, onto the metal substrate. The most common method to achieve this step is photolithography. However, this study introduces ink-jet technology, which allows for direct deposition only in the areas that need to be covered, thus avoiding both the “resist stripping” phase and the waste of photoresist. Subsequently, the masked sample undergoes anodic polarization, typically controlled galvanostatically, where the current level is set based on the desired removal rate or final etching depth. Previous studies suggest that pulsed current mode may enhance surface finish and discourage the deposition of corrosive products on the etched surface [25,26]. Furthermore, galvanic regulation must be considered in relation to other components of the electrochemical cell used, particularly the electrolyte in which the sample is immersed and the spatial arrangement of the counter electrode. Indeed, the solution can serve as a simple conductive electrolyte, but it can also be modified by adding complexing agents to improve the removal of cations produced by the anodic reactions or, alternatively, exploit additional etching effects by introducing acids or bases in the case of an amphiphilic material like aluminum. Furthermore, the resistance of the polymeric mask in the electrolyte and its adhesion for a treatment time suitable for the planned etching degree must be taken into account. In the case of aluminum alloys with significant concentrations of alloying elements, as in the case of copper in AA2024-T3, the choice of the electrolyte can be complex.

This complexity arises from the need to consider the various corrosion products that will form, as well as potential localized corrosive attacks in microstructural heterogeneities at the metal surface, typically resulting in pitting corrosion [27]. AA2024-T3, renowned for its strength and fatigue resistance, is extensively utilized in aeronautical applications [28,29]. However, despite its excellent mechanical properties, it exhibits lower corrosion resistance compared to pure metal [30,31] and this feature could alter also the etching stage of texture production.

1.3. Aim of the work

In this context, this study investigated the influence of different processing parameters, including the ink-jet-based mask deposition and metal electrochemical etching, on the riblet-textured surface profile. A real-scale geometry derived from a fluid dynamics study specific to low-speed conditions was considered. The key technological parameters were discussed and optimized including ink-jet strategies for mask production, etching solutions, treatment time, and the features of applied anodic current. The experimental results provided insights into TMEMM for fabricating complex structures on AA2024-T3 for structural engineering applications. Ultimately, this research aimed to provide a valuable technological tool for tailored texturing of aluminum alloys, enhancing their performance in aeronautical and related industries. The obtained texture was systematically studied through cross-sectional observation using a scanning electron microscope (SEM), followed by an analysis of the geometric parameters obtained. These data were correlated with the production parameters.

2. Materials and methods

2.1. Profile definition

In this study, the applicability of TMEMM technology in replicating the textured structure of mako shark skin is evaluated. An ideal geometry profile is considered to provide an effective drag reduction for the fluid dynamic conditions typical of a low-speed aircraft, such as an unmanned aerial vehicle (UAV), or an aircraft during takeoff and landing phases. This application requires surface texturing composed of a pattern of riblets organized in straight lines of specified pitch (s) and height (h) depicted in Fig. 2, depending on the position of the vehicle and on the flow field around the body [32,33]. Since the optimal local profile varies for each spot on the aircraft, for this study some plausible parameters reported in a related study on a fixed-wing drone have been considered [32]. The optimal riblets spacing can be defined as dimensionless with viscous unit as:

$$s^+ = s \cdot u_T / \nu \tag{1}$$

which can be used to express the physical riblet spacing s in terms of the fluid viscosity ν, which is in general easily known for applications, and the friction velocity $u_T = \sqrt{T_w \cdot \rho}$; T_w and ρ represent the friction at the solid wall and the fluid's density respectively. Garcia-Mayoral et al. [34] identified the optimal drag breakdown performances for the parameter s^+equal to 15. Moreover, taking as reference some characteristic quantities, taken from the work by Cacciatori et al. [32] and valid for a specific fixed-wing drone such as wing chord at root L = 0.3 m, cruise speed U = 25 m/s, air density at sea level $\rho = 1.225$ Kg/m^3, air dynamic viscosity at sea level $\nu = 1.8 \times 10^{-5}$ Pa • s, it has been obtained a global Reynolds number $\mathrm{Re} = \rho\, L\, U/\mu \approx 5 \cdot 10^5$. At this point, by means of the theory of the laminar Blasius boundary layer over a flat plate, the parameter T_w can be estimated and accordingly also the optimum spacing s. The authors identified for such conditions, the optimal peak-to-peak riblets spacing stood around 200 μm in most areas of the drone except for the trailing edge of the wing and the aft part of the fuselage, and so taking this value constant would yield drag reduction very close to the maximum achievable. Similarly, in the considered case, the computed riblet height is predominantly around 100 μm [32]. The reported data refers to a standard V-groove profile shape, which could likely vary to a semi-elliptical one when dealing with electrochemical-based production. However, the current knowledge is that the detailed shape of the cross-section is not crucial, but its dimensions are [6]. Considering these facts, in this study these geometric parameters have been used as target values that can vary significantly depending on fluid dynamic assumptions and aircraft geometry. However, despite the dimensions being only indicative references and the riblet profile shape seemingly not significantly affecting performance, the sharpness of their tip is crucial. This constraint poses challenges for riblet production parameter optimization and maintenance scheduling, both fundamental aspects in aeronautical applications.

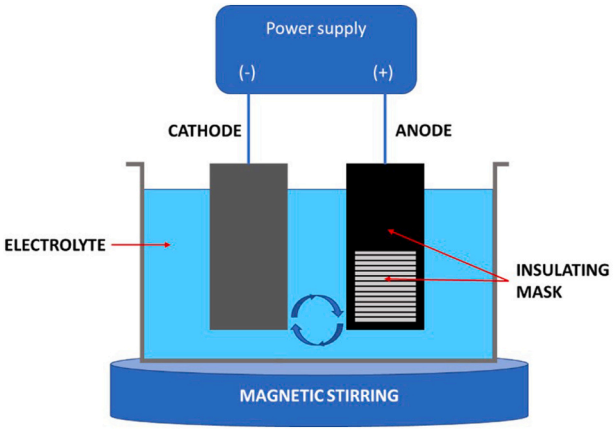

Fig. 3. Through-mask electrochemical micromachining setup scheme.

2.2. Texture production by TMEMM

The AA2024-T3 Al-Cu-Mg alloy (Cu 3.8–4.9 wt%, Mg 1.2–1.8 wt%, Si max. 0.5 wt%, Fe max. 0.5 wt%, Zn max. 0.25 wt%, Mn 0.3–0.9 wt%, Al Bal.) [35], widely used in aeronautical applications, is selected for this project due to its real-world applicability and the challenges it poses in ensuring durability against atmospheric agents, particularly from the corrosion behavior standpoint [36]. The texture on the metallic surface is achieved through a two-step treatment process. The deposition of a masking layer of dielectric material using ink-jet technology is followed by an electrochemical etching, carried out by applying an anodic current to the unmasked surface aluminum area [22,26].

The metal sheets are cleaned through sonication in acetone before mask printing for 10 min. Any pickling pre-treatment is discarded as it was found to increase substrate wettability, complicating the precise control of ink deposition and the splatting diameter of the ink droplets. A CERADROP F-Series (MGI group) ink-jet printer equipped with UV-curing acrylic-based dielectric ink is used. A pattern of parallel straight lines with a width of 120 μm and a pitch of 200 μm is achieved using a Samba Cartridge (Fujifilm Dimatix) based on Si-MEMS, which provides a native drop volume of 2.4 pL which displays a wet diameter on the AA2024-T3 surface of 80 μm. A filling strategy based on a 50 % overlap of individual ink droplets is chosen along with a UV curing protocol after each printing layer. Initially, masks composed of 10 layers of dielectric material were considered, and later the mask thickness doubled.

The samples onto which the mask is deposited undergo electrochemical etching in a two-electrode electrochemical cell (schematized in Fig. 3), wherein the sample served as the working electrode and a titanium mesh acted as the counter electrode. The electrodes are planar and parallelly placed with a constant relative distance of 2 cm. Both electrodes are immersed in a 1.17 M sodium nitrate solution (pH 5.7) magnetically stirred. Using a Delta Elektronika SM1500 series power

Table 1
Experimental parameters evaluated during the TMEMM process.

TMEMM electrolyte	Direct current supply (A/cm^2)	Pulsed current supply (A/cm^2)	Pulsed duty cycle (%)
1.17 M $NaNO_3$	1, 1.5, 2, 2.5, 3	2	25, 50
1.17 M $NaNO_3$ + 0.1 M EDTA	2	–	–
1.17 M $NaNO_3$ + 0.5 M Glycine	2	–	–
1.17 M $NaNO_3$ + 0.1 M Ammonia	2	–	–

supply, tests at various intensities of continuous anodic current are conducted (from 1 to 3 A/cm^2), varying treatment times. Moreover, a 2 A/cm^2 pulsed current (on/off) characterized by a frequency of 250 Hz is applied to a parallel collection of samples changing its duty cycle (d.c.%) from 50 % to 25 %. The addition of a complexing agent such as Ethylenediaminetetraacetic acid (EDTA) at a concentration of 0.1 M, 0.5 M of glycine, and 0.1 M of ammonia is evaluated to limit chemical compounds deposition on the sample surface during treatment [37,38]. The experimental variables are listed in Table 1.

The main variables present in both phases are evaluated, such as the orientation of the mask with respect to the rolling direction of the substrate metal, the intensity of the applied anodic current, and the etching time. The profiles obtained under various combinations of parameters are observed in cross-section via SEM (Jeol-Japan JSM-IT300), and the geometric parameters are discussed in relation to the optimal profile derived from the fluid-dynamic consideration. Fig. 4 defines the geometrical parameters considered during etching evolution. The etching depth is described by the parameter *h,* the peak-to-peak distance of riblets pitch by *s,* the elliptical etched cavity by major diagonal by letter *w,* and the width of the riblet flat-head by *T.* Notice that when T → 0, the profile turns into a cusp like profile resembling shark skin scale [39].

3. Results

3.1. Direct current etching

Initially, the morphology of the mask pattern obtained from dielectric ink printing was studied. The simplest case of a pattern of lines characterized by a width of 120 μm and pitch of 200 μm was considered. Fig. 5 is a top view of the lines obtained by printing the mask perpendicular and parallel, respectively, to the rolling direction, identifiable by the striations on the metal surface. In the case where the lines are aligned parallel to the rolling direction (Fig. 5b), the distribution in the organic material results in more homogeneous and dimensionally reproducible compared to the case in which the lines are printed normally (Fig. 5a). This would translate into a better quality in the geometry of the riblets obtained after etching. In Fig. 6, it is appreciated at various magnifications how discontinuities in the masking layer produce a non-uniform etched profile shifting longitudinally along the sample (Fig. 6a and Fig. 6c). Based on these results, it was decided to proceed with the study of samples with printed ink lines parallel to the rolling direction. No significant inhomogeneities in etching due to the distribution of intermetallics are observed. The printing and anodizing parameters have a predominant influence over the local contribution of intermetallic particles. The electrochemical and microstructural behavior resulting from micromachining will be addressed in a separate publication, as this study focuses on achieving texturing from a profilometric perspective. Regarding the choice of line width, beyond 120 μm, a frequent smudging effect is observed during printing, resulting in areas where the pattern becomes indistinguishable. The need to have enough large (in width) mask lines aligns with the need to achieve, after the subsequent etching, grooves having a depth comparable to the distance between the peaks of the riblets. Such a result is unattainable with narrow lines, which tend to detach prematurely during the initial stages of anodic polarization of the sample.

The parameters involved in the electrochemical etching phase were

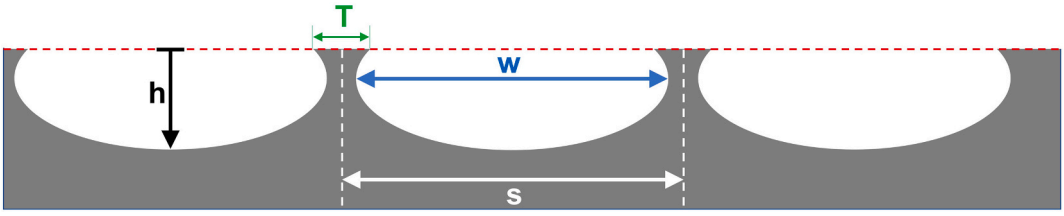

Fig. 4. Schematic depiction of the defining geometrical dimensions during through-mask etching of a metal substrate: riblets pitch (s), maximum etch depth (h), riblets head width (T), elliptical etch cavity major diagonal (w).

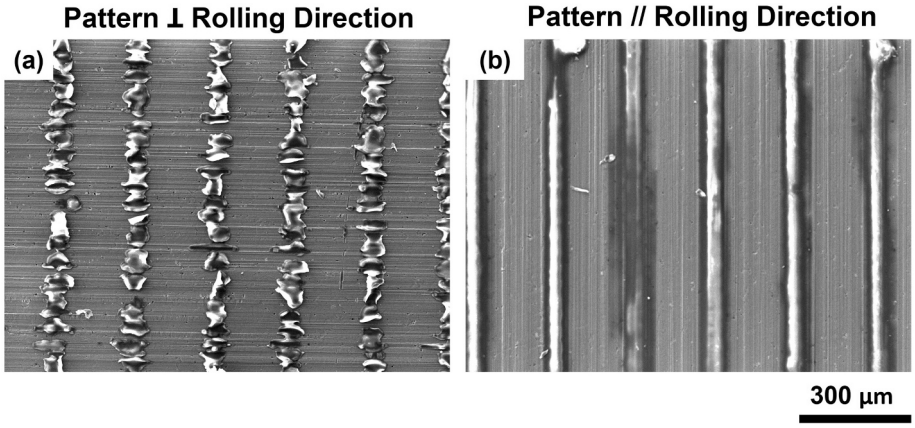

Fig. 5. SEM-SED top view of the ink-jet printed mask on aluminum AA2024-T3 surface. The image shows the acrylic-based lines after UV-curing in two pattern configurations: (a) orthogonal and (b) aligned to the rolling direction.

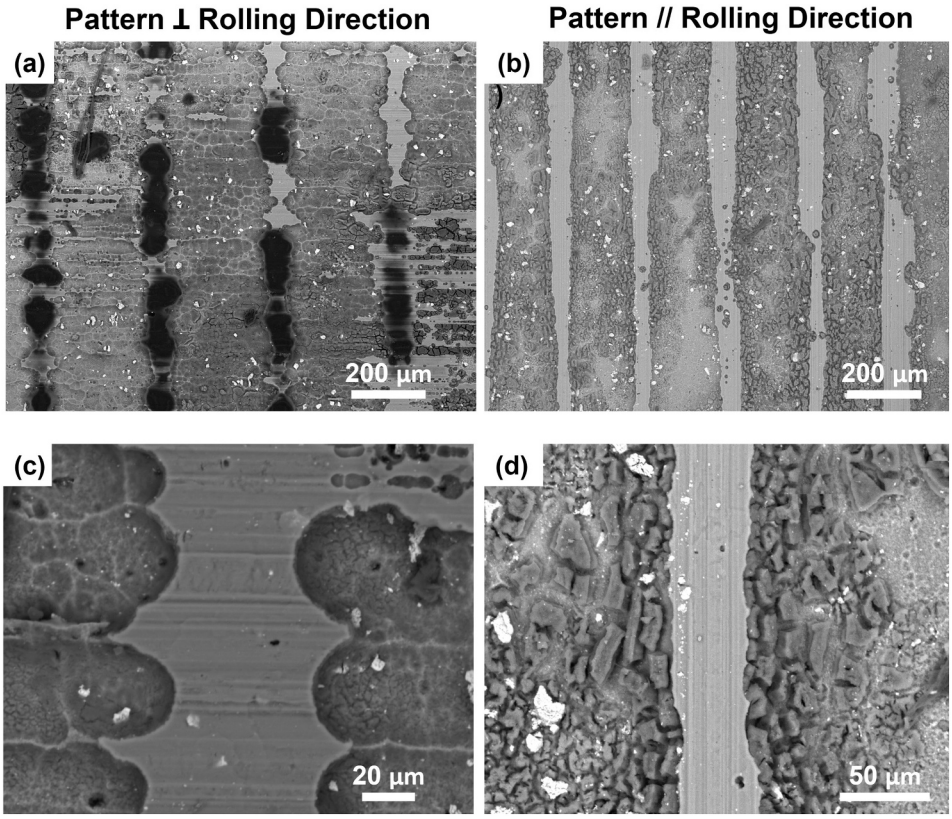

Fig. 6. SEM-BED top view of two different etched surfaces after the same treatment route. The comparison of the outcomes starting from similar masking patterns (s = 200 µm) printed (a, c) orthogonally and (b, d) parallelly to the aluminum plates rolling direction is displayed.

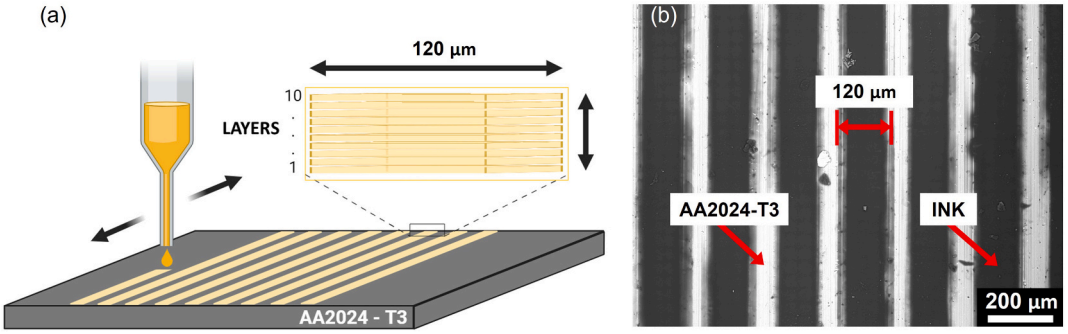

Fig. 7. Scheme of the multiple layers ink-mask deposition on an AA2024-T3 panel (a), and the SEM-BED top-view of the obtained masking pattern of pitch 200 µm and line-width of 120 µm (b).

initially studied using masks composed of 10 layers of cross-linked acrylic ink (Fig. 7). These surfaces were treated in galvanostatic mode with currents of intensities 1, 1.5, 2, 2.5, and 3 A/cm^2. For each current level, several treatment times were compared in such a way as to keep the same 5 values of current density applied per etching time constant for each current. Following this concept, the results are presented in function of the product between current density and etching time, namely "etching degree". The profiles of the riblets obtained are shown in Fig. 8. Given the ideal profile from a fluid dynamics perspective, as sharp as possible, it is noted that similar shapes are achievable regardless of the value of the anodic current. Except for the extreme cases of 1 A/cm^2, which seem to be too mild, in the other cases (1.5, 2, 2.5, and 3 A/cm^2), the best profile is obtained after 240, 180, 144, and 120 s, respectively, parameters that correspond at a common etching degree of 360 A·s/cm^2. At longer treatment times, over-etching occurs, leading to a decrease in riblet height. In the four mentioned cases, the depth of the groove, or alternatively the height of the riblets *h*, ranges between 50 and 70 µm (Fig. 9a), a value that at this point does not meet the optimal target for the considered case of study, but could be anyway a possible optimum profile considering a diverse application spot on low-speed aerial vehicle or the velocity of a more general aircraft [32].

Regarding the etching penetration rates in the vertical direction, it remains constant until the cusp-shape point (condition when T tends to zero) is reached. Furthermore, it is dependent on the applied anodic current density, following the second-order polynomial fitting curve shown in Fig. 9b. Beyond a specific intensity, the oxidation reactions occurring on the surface of the aluminum alloy reach a kinetically limiting state, achieving a maximum penetration rate of 0.32 µm/s. This rate is significantly higher (by 2 orders of magnitude) compared, for instance, to chemical etching on the same AA2024-T3 alloy [40], and one order of magnitude increased with respect to similar TMEMM on pure aluminum [25,26].

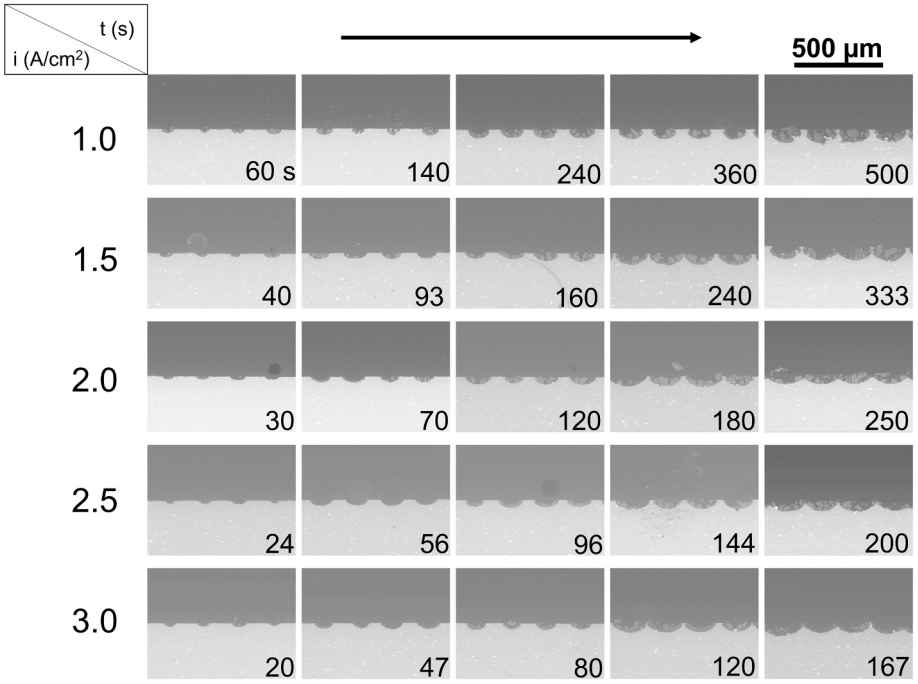

Fig. 8. Etching optimization study on a printed lines-pattern of pitch s = 200 µm.

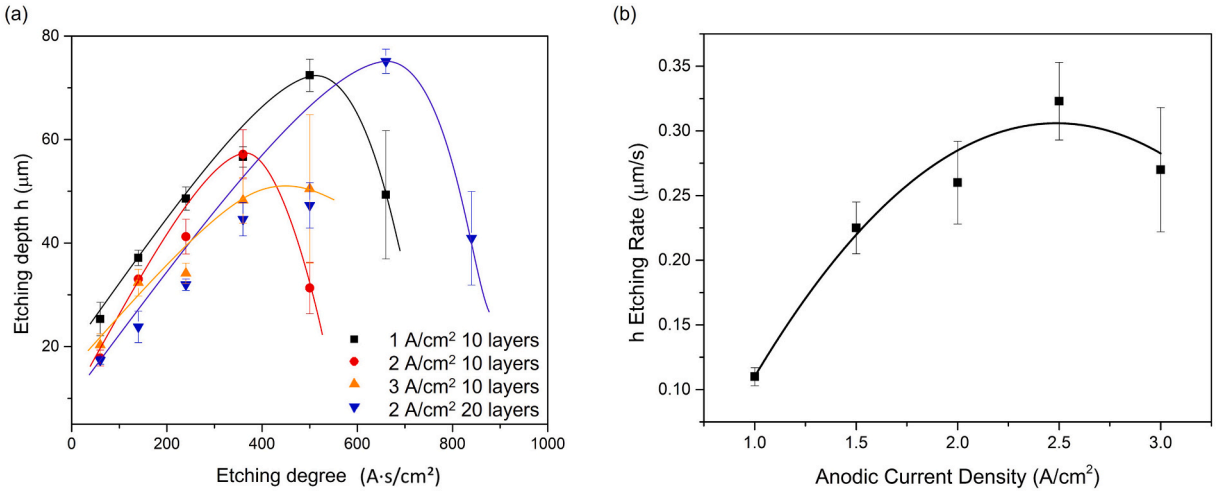

Fig. 9. Etching depth (h) evolution at increasing the product of the etching time-on and the current intensity, namely "Etching Degree" (A·s/cm^2) (a), and the dependence of the vertical etching rate on the applied anodic current density (b). Profiles obtained applying continuous current in 1.17 M $NaNO_3$.

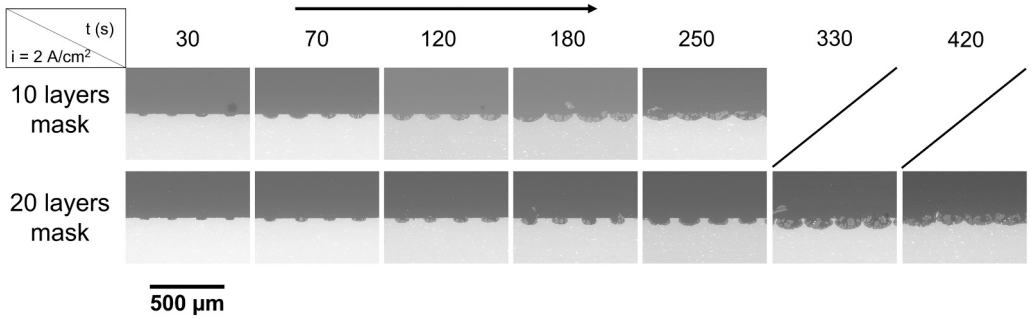

Fig. 10. Etched profiles comparison of two different ink-jet printed masks (same pattern pitch s = 200 µm) where the bottom one has the double number of printed layers overlaid. The delay effect in obtaining the optimum sharp peak shape increasing the thickness of the shielding mask is displayed. Profiles obtained applying continuous current in 1.17 M $NaNO_3$.

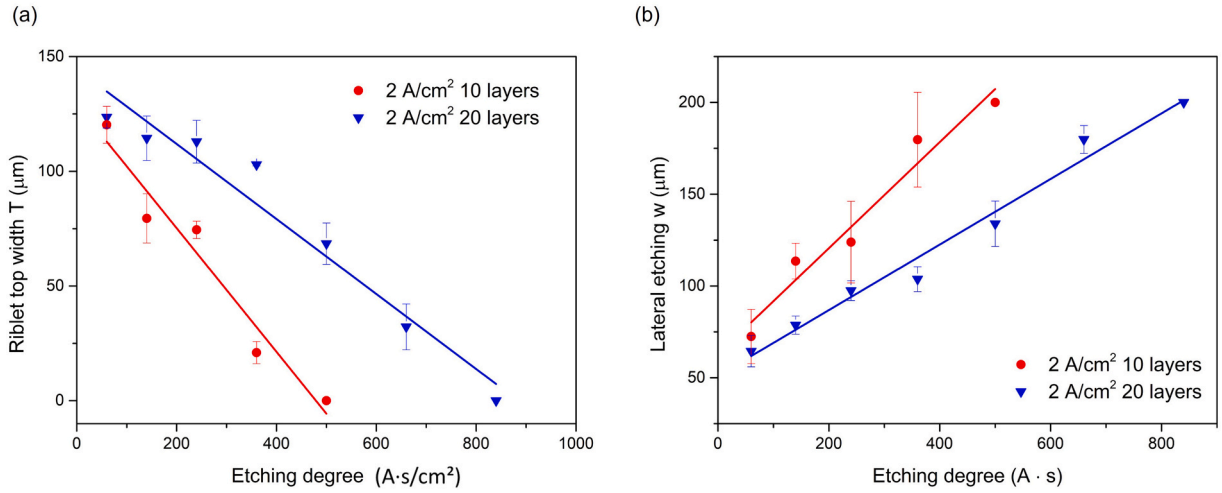

Fig. 11. Riblet top head width (T) and lateral etching (w) evolution at increasing the product of the etching time-on and the current intensity, namely "Etching Degree" (A·s/cm^2). Samples masked with 10 and 20 ink layers are compared. All profiles were obtained by applying continuous current in 1.17 M $NaNO_3$.

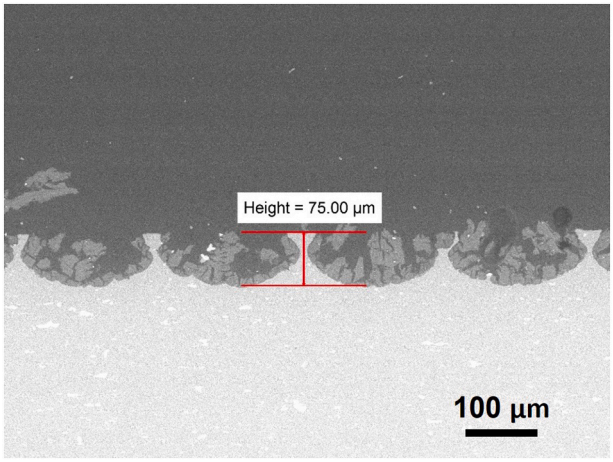

Fig. 12. Etched profile obtained from a pattern pitch s = 200 μm and 20 ink-layers after 330 s etching at 2 A/cm^2. The riblet's height measurement is displayed around 75 μm.

At this point, to overcome the limit encountered in obtaining deeper grooves, several strategies have been tested to check the working range of the applied TMEMM technology. Firstly, a test with a mask composed of twice the number of layers compared to the case studied in Fig. 8 (from 10 to 20 layers) was conducted. Increasing the thickness of the masking layer delays the achievement of the optimal sharp profile (Fig. 10) concurrently to a slower lateral consumption *w* (Fig. 11b). The thicker mask seems to provide enhanced protection in terms of mask-detaching delay and metal-polymer interface protection, likely due to the more compact layer deposited. Despite this being the desired effect of applying such a strategy, it did not translate into significantly deeper etching grooves for longer treatment times. However, by this approach riblets 75 μm high have been produced, despite a frequent loss of sharpness in the tip profile as represented by the higher *T* value (riblet top head width) during the entire etching, as visible in Fig. 11a. The resulting riblet shape is captured in Fig. 12, where the presence of residual oxidation products on the surface profile after treatment is also displayed, which can be easily removed by ultrasonic cleaning procedure. No undesired etching effects were observed as long as the mask remained well-adhered to the aluminum surface. The only under-etching phenomenon detected was the undercut, which was not a drawback but rather an effect intentionally leveraged and controlled to achieve the optimal surface profile. This controlled undercutting proved to be fundamental in shaping the desired texture.

This result states that a technological restriction is present in these experimental conditions. Despite it deviates from the example of optimal value reported in Section 2.1 by about 25 %, this profile still provides a drag reduction effect compared to the flat surface and indeed could be the optimum profile in another location of the vehicle [6]. However, from the TMEMM technology point of view, this is a limitation, which is presumed to be the result of multiple effects, among which the main ones may include a shielding effect caused by deposits of corrosion products in the area where selective forced corrosion would occur (mainly copper, aluminum, and magnesium oxides), and a typical tip effect, namely the concentration of the electric field at the apex of the riblets, resulting in accelerated etching in these areas.

The case of the polymeric mask with a double number of ink layers (20 layers) has been explored to assess the technological boundaries of this production procedure, particularly in terms of etching depth, or in other words, the height of the riblets obtained. However, this results in a deterioration in the regularity of the profile and in greater difficulty in obtaining a sharp riblet since the increased etching time enabled by the thicker mask causes a greater lateral consumption effect, exceeding the possibility of achieving the desired sharp peak profile, which is actually the main shape requirement.

3.2. *Use of complexing agents*

Two more strategies to counteract the progressive deposition of corrosion products on the surface have been studied. The first is based on the introduction of a compound with complexing action into the electrolyte. EDTA was chosen for its ability to form complexes with many metal cations in a 1:1 ratio regardless of the oxidation state of the ion [37]. Ammonia and glycine are the other two compounds explored for electrolyte modification. It is well known that glycine is an effective complexing agent frequently used to enhance the reduced removal rate [41,42].

The addition of EDTA at a concentration of 0.1 M acidifies the solution to a pH of 4.7, making the electrolyte more aggressive towards the metal substrate of an amphoteric nature under consideration. However, this does not result in a greater etching depth h as highlighted in Fig. 13a. Moreover, it seems to alter the shape of the profile: the ideal fluid dynamics sharp shape is replaced by a lateral marked undercut that forms in the riblet, resulting in a "T"-shaped apex (Fig. 12).

In the scenario, other complexing agents were tested singularly. Glycine (0.5 M) was introduced in the base 100 g/L $NaNO_3$ solution as a

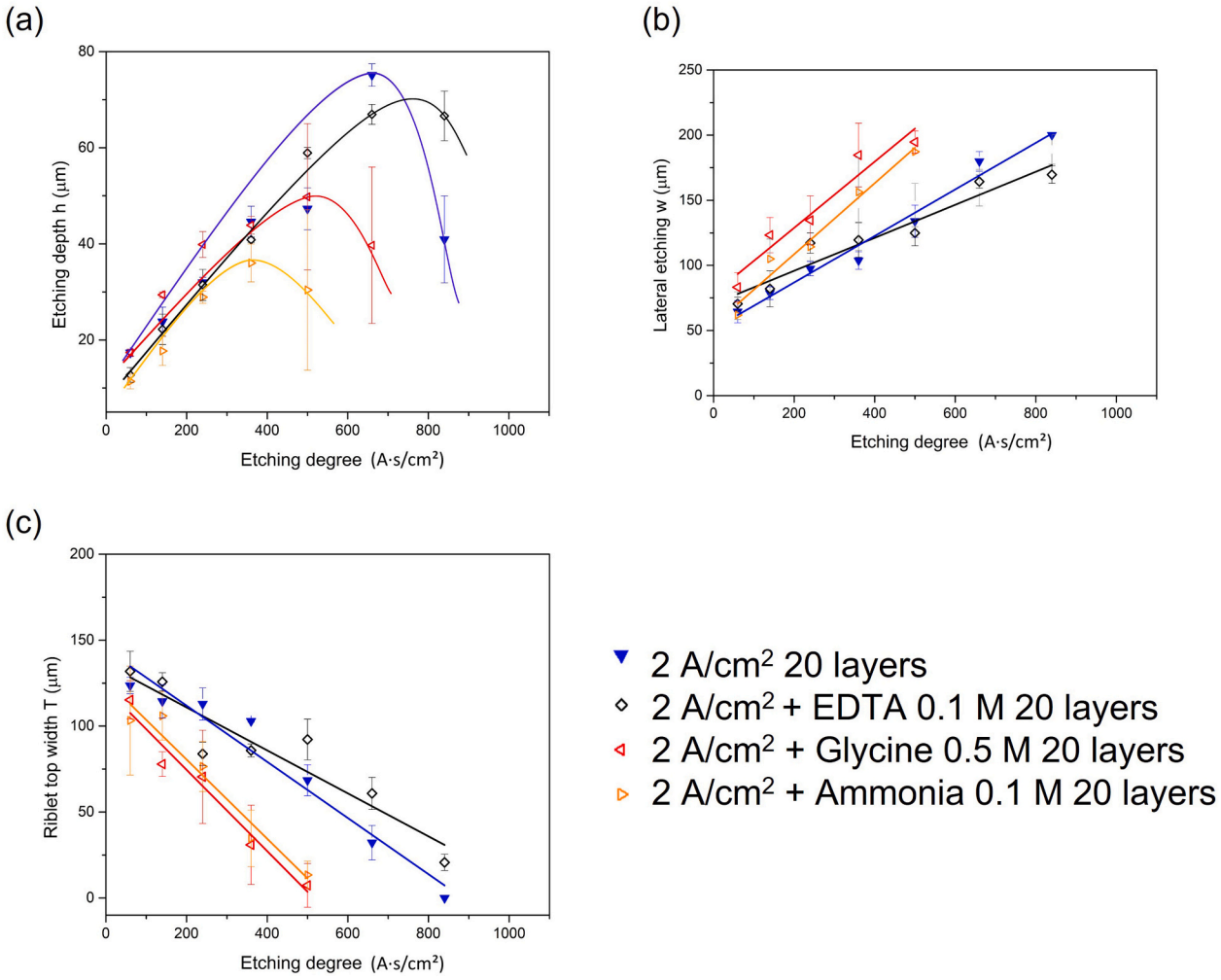

Fig. 13. Riblets geometrical parameters evolution at increasing the product of the etching degree (A·s/cm^2): etching depth h (a), lateral etching w (b), and riblets head top width T (c). The behavior of samples produced by a 20 ink-layers masking is displayed varying the etching electrolytes.

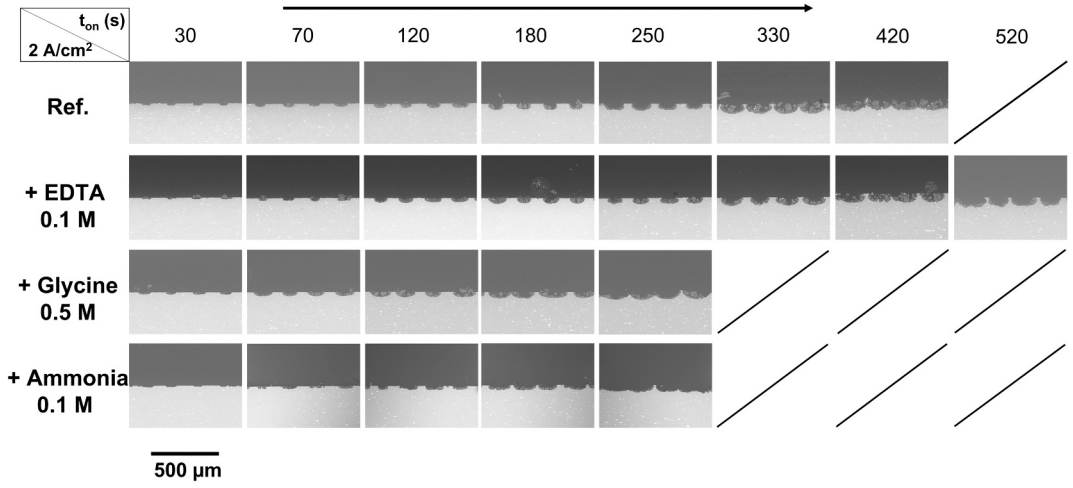

Fig. 14. Etched profiles comparison of the same masking pattern (pitch s = 200 μm and 20 ink layers) in different treatment conditions: continuous current in 1.17 M $NaNO_3$, continuous current in 1.17 M $NaNO_3$ with the addition of 0.01 M of EDTA, glycine 0.5 M, and ammonia 0.1 M.

complexing agent for aluminum ions [41,42], with the anticipated goal of augmenting the etching removal rate and improving the surface finishing, the outcomes achieved were rather dissatisfactory (Fig. 14). Under this nearly neutral solution condition (pH 6), the advancement of grooves appears to be less prominent in depth h (Fig. 13a) compared to the reference case without any addition, while lateral evolution (w) seems to predominate over all the other cases of study (Fig. 13b). The introduction of this complexing agent does not appear to compensate for

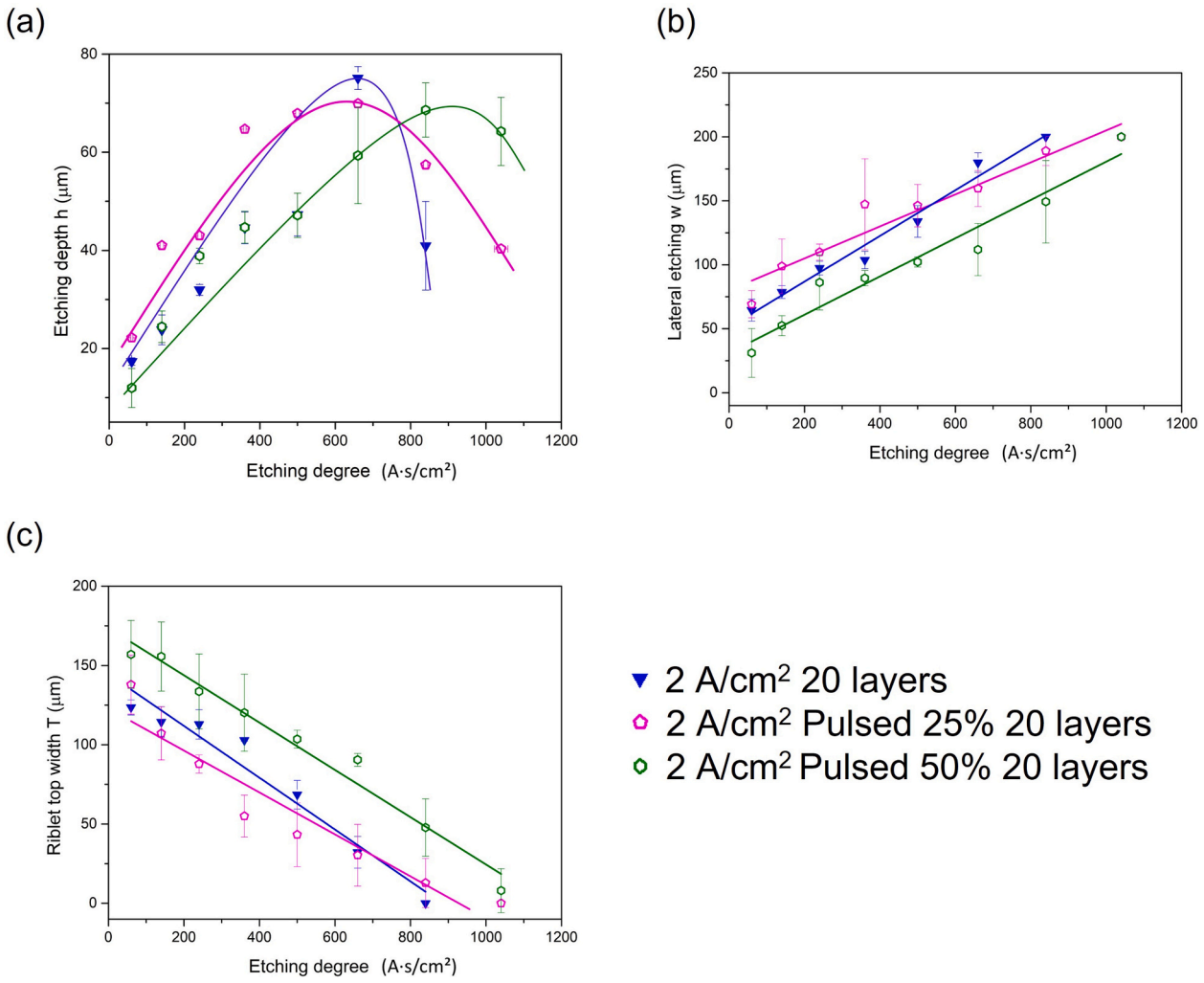

Fig. 15. Riblets geometrical parameters evolution at increasing the product of the etching degree (A·s/cm^2): etching depth h (a), lateral etching w (b), and riblets head top width T (c). The behavior of samples produced by a 20 ink-layers masking is displayed varying the etching current supply signal.

the "masking" effect of corrosion products in the grooves, or this phenomenon is not the primary limitation in advancing etching in the depth direction. Indeed this augmented aggressivity of the etching aligns with previously published experimental data where an increase in glycine concentration causes a sharp rise in the removal rate [43]. Researchers indicate that glycine molecules can form complexes with metal ions, such as aluminum ions and aluminum oxide, resulting in soluble glycine-aluminum products [41,42].

Furthermore, by adding ammonia in a concentration of 0.1 M, an alkalinization of the etching environment is triggered to pH 11. Even in this case, a more pronounced profile is not obtained. Instead, these conditions produce riblets with a height h smaller than those produced under other conditions, given the same applied current. Additionally, the shorter peaks are characterized by a greater lateral consumption w and an early loss of the polymer mask shielding, as evidenced by the more rapid and premature decline of the parameter T. Therefore, the modification of the electrolyte and the alteration of the pH make the conditions more aggressive for the metal. However, this simultaneously damages the texturing process by diminishing the selectivity of the attack in the unmasked areas. By adjusting the discussed parameters to correctly proportion the lateral consumption w relative to the depth, it is possible to meet the most important requirement for the application in question, namely the pointed shape of the riblets. Consequently, chemical alterations to the electrolyte that lead to either excessive aggressiveness, prematurely undermining the mask-substrate interface, or an accelerated lateral consumption w relative to the reduction of the riblet top width T, should be avoided in the process of optimizing the production process.

3.3. *Pulsed current etching*

Pulsed current electrochemical etching was also employed to try to obtain the desired profile. Pulsed current consists of an on-time followed by a period during which no current is applied. These steps are regulated by the so-called duty cycle, which defines the portion of time during which current is applied relative to the total period. In this way, by applying 2 A/cm^2 with a 50 % duty cycle at a frequency of 250 Hz, a current delivery profile is obtained in which 2 μs of polarization are alternated with 2 μs of cell off. During this off-period, the stirring effect should facilitate the removal of corrosion products and restore the equilibrium and concentrations of chemical species at the interface [26]. With this second approach based on pulsed current, the treatment time was chosen considering the "on" time in order to have periods of selective corrosion comparable to the ones previously used, reported in Fig. 14. This approach leads to promising results, confirming the fact of being favored as a preferable method in related studies found in the literature [26]. In this case, achieving maximum riblet height appears to be less dependent on the treatment time choice (Fig. 15). Comparing it with a similar case under continuous current, a sharp drop after the maximum height is not observed in Fig. 15a but rather a more gradual

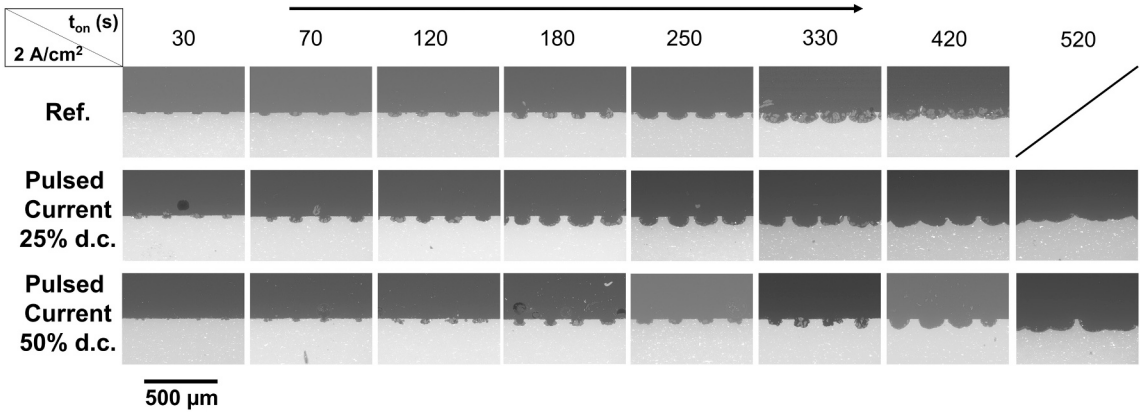

Fig. 16. Etched profiles comparison of the same masking pattern (pitch s = 200 µm and 20 ink layers) in different treatment conditions: continuous current in 1.17 M $NaNO_3$, and pulsed current (duty cycle 50 %, 250 Hz) in 1.17 M $NaNO_3$.

trend for both the duty cycles tested. This behavior may suggest that pulsed current offers greater adaptability to potential industrial processes, resulting in less variability in the obtained profiles in terms of etching depth (Fig. 16). However, to obtain profiles similar to those produced by direct current, doubled treatment times are necessary, considering a 50 % duty cycle. Regarding the surface finishing obtained under different electrolyte conditions, no significant differences were observed when varying the process parameters. The arithmetic mean roughness (*Ra*) was consistently around 0.86 ± 0.03 µm when measured on flat-etched substrates. However, this value increased significantly due to the TMEMM process, showing a 40 % rise compared to the untreated AA2024 surface. While this roughness variation could influence the drag reduction properties, the riblet geometry is undoubtedly the dominant feature in this context.

4. Conclusions

This study demonstrates how TMEMM technology, based on mask patterning via ink-jet, can be engineered to modulate the riblet pattern pitch along different areas of the aircraft characterized by varying fluid dynamics conditions. With this technology, it is possible to meet the most important requirement for the considered drag-reduction purpose, which is the pointed shape of the riblets.

Furthermore, by leveraging the electric field in electrochemical etching through the shape, the period of treatment, and masking features the height of the riblets—i.e., the depth of the etching—can be tailored according to the needs of the optimal design. In this context, a vertical etching rate in the order from 0.11 to 0.32 µm/s is displayed at different levels of static anodic polarization achieving the maximum riblet's height of 75 ± 2 µm when etching at 2 A/cm^2 for 330 s a AA2024-T3 substrate masked with a 20 ink-layers 200 µm spaced pattern.

Generally, a thicker layer of the applied polymeric mask provides more opportunities to go deeper with longer etching before observing a decrease in riblet height due to over-etching.

The addition of complexing agents such as EDTA, glycine, and ammonia, does not seem to have relevance to the profile or final surface finish.

Similarly, pulsed current as an alternative to direct current is expected to facilitate the removal of corrosion products generated on the surface during etching. However, this does not result in a significant effect on the evolution of the geometry of the obtained profiles.

The ultimate challenge lies in optimizing the parameters to obtain both riblets of adequate height and sharp profiles, shapes achievable at a precise moment during the etching treatment, just before the loss of riblet height occurs. The industrial scalability of TMEMM could be promising, as high-current electrochemical processes are already well-established. However, upscaling requires careful thermal management to maintain electrolyte stability and process efficiency. Future developments should focus on optimizing bath configuration and temperature control to address potential heating issues. Despite these challenges, TMEMM remains a viable approach for large-area surface texturing in industrial applications.

CRediT authorship contribution statement

Andrea Cristoforetti: Writing – review & editing, Writing – original draft, Methodology, Investigation, Data curation, Conceptualization. **Matteo Gamba:** Writing – review & editing, Validation. **Andrea Brenna:** Writing – review & editing, Validation, Project administration, Funding acquisition, Conceptualization. **Marco Ormellese:** Writing – review & editing, Validation, Project administration, Conceptualization. **Michele Fedel:** Writing – review & editing, Validation, Project administration, Funding acquisition, Conceptualization.

Declaration of competing interest

The authors declare that they have no known competing financial interests or personal relationships that could have appeared to influence the work reported in this paper.

Acknowledgments

The authors acknowledge funding by EUROPEAN UNION – NEXT GENERATION EU, PNRR - MISSIONE 4 “ISTRUZIONE E RICERCA” - COMPONENTE C2 INVESTIMENTO 1.1 “FONDO PER IL PROGRAMMA NAZIONALE DI RICERCA E PROGETTI DI RILEVANTE INTERESSE NAZIONALE (PRIN)” D.D. N. 104/2022 “BANDO PRIN 2022”. PE11 Engineering of Metals and alloys.

AC and MF acknowledge the Italian Ministry of Education, University and Research (MIUR) and the Department of Industrial Engineering of the University of Trento (DII) for funding support under the “Department of Excellence” program 2018-2022.

Data availability

Data will be made available on request.

References

[1] A.A.G. Bruzzone, H.L. Costa, P.M. Lonardo, D.A. Lucca, Advances in engineered surfaces for functional performance, CIRP Ann. 57 (2008) 750–769, https://doi.org/10.1016/j.cirp.2008.09.003.

[2] T. Singh, A. Dvivedi, Developments in electrochemical discharge machining: a review on electrochemical discharge machining, process variants and their hybrid

methods, Int. J. Mach. Tools Manuf. 105 (2016) 1–13, https://doi.org/10.1016/j.ijmachtools.2016.03.004.
[3] B. Dean, B. Bhushan, Shark-skin surfaces for fluid-drag reduction in turbulent flow: a review, Phil. Trans. R. Soc. A 368 (2010) 4775–4806, https://doi.org/10.1098/rsta.2010.0201.
[4] X. Pu, G. Li, Y. Liu, Progress and perspective of studies on biomimetic shark skin drag reduction, ChemBioEng Reviews 3 (2016) 26–40, https://doi.org/10.1002/cben.201500011.
[5] K. Fukagata, K. Iwamoto, N. Kasagi, Contribution of Reynolds stress distribution to the skin friction in wall-bounded flows, Phys. Fluids 14 (2002) L73–L76.
[6] R. García-Mayoral, J. Jiménez, Drag reduction by riblets, Phil. Trans. R. Soc. A 369 (2011) 1412–1427, https://doi.org/10.1098/rsta.2010.0359.
[7] M. Walsh, L. Weinstein, Drag and heat-transfer characteristics of small longitudinally ribbed surfaces, AIAA J. 17 (1979) 770–771.
[8] D.W. Bechert, M. Bruse, W. Hage, J.G.T. Van Der Hoeven, G. Hoppe, Experiments on drag-reducing surfaces and their optimization with an adjustable geometry, J. Fluid Mech. 338 (1997) 59–87, https://doi.org/10.1017/S0022112096004673.
[9] P. Luchini, F. Manzo, A. Pozzi, Resistance of a grooved surface to parallel flow and cross-flow, J. Fluid Mech. 228 (1991) 87–109.
[10] S. Endrikat, D. Modesti, M. MacDonald, R. García-Mayoral, N. Hutchins, D. Chung, Direct numerical simulations of turbulent flow over various riblet shapes in minimal-span channels, Flow Turbulence Combust 107 (2021) 1–29, https://doi.org/10.1007/s10494-020-00224-z.
[11] A. Sareen, R.W. Deters, S.P. Henry, M.S. Selig, Drag reduction using riblet film applied to airfoils for wind turbines, Journal of Solar Energy Engineering 136 (2014) 021007.
[12] Y.F. Fu, C.Q. Yuan, X.Q. Bai, Marine drag reduction of shark skin inspired riblet surfaces, Biosurface and Biotribology 3 (2017) 11–24, https://doi.org/10.1016/j.bsbt.2017.02.001.
[13] X. Pu, G. Li, H. Huang, Preparation, anti-biofouling and drag-reduction properties of a biomimetic shark skin surface, Biology Open 5 (2016) 389–396.
[14] W. Choi, C. Lee, D. Lee, Y.J. Won, G.W. Lee, M.G. Shin, B. Chun, T.-S. Kim, H.-D. Park, H.W. Jung, Sharkskin-mimetic desalination membranes with ultralow biofouling, J. Mater. Chem. A 6 (2018) 23034–23045.
[15] M.K. Gabler-Smith, D.K. Wainwright, G.A. Wong, G.V. Lauder, Dermal Denticle diversity in sharks: novel patterns on the interbranchial skin, Integrative Organismal Biology 3 (2021) obab034, https://doi.org/10.1093/iob/obab034.
[16] W. Dai, M. Alkahtani, P.R. Hemmer, H. Liang, Drag-reduction of 3D printed shark-skin-like surfaces, Friction 7 (2019) 603–612.
[17] N. West, K. Sammut, Y. Tang, Material selection and manufacturing of riblets for drag reduction: an updated review, Proceedings of the Institution of Mechanical Engineers, Part L: Journal of Materials: Design and Applications 232 (2018) 610–622, https://doi.org/10.1177/1464420716641452.
[18] M.H. Kwon, H.S. Shin, C.N. Chu, Fabrication of a super-hydrophobic surface on metal using laser ablation and electrodeposition, Appl. Surf. Sci. 288 (2014) 222–228, https://doi.org/10.1016/j.apsusc.2013.10.011.
[19] Y. Liu, L. Moevius, X. Xu, T. Qian, J.M. Yeomans, Z. Wang, Pancake bouncing on superhydrophobic surfaces, Nat. Phys. 10 (2014) 515–519, https://doi.org/10.1038/nphys2980.
[20] S. Cho, R. Tummala, Y. Joshi, Capillary performance of micropillar arrays in different arrangements, Nanoscale and Microscale Thermophysical Engineering 22 (2018) 97–113, https://doi.org/10.1080/15567265.2018.1431749.
[21] K.K. Saxena, J. Qian, D. Reynaerts, A review on process capabilities of electrochemical micromachining and its hybrid variants, Int. J. Mach. Tools Manuf. 127 (2018) 28–56, https://doi.org/10.1016/j.ijmachtools.2018.01.004.
[22] T. Baldhoff, V. Nock, A. Marshall, Through-mask electrochemical micromachining, J. Electrochem. Soc. 165 (2018) E841.
[23] T. Kikuchi, Y. Wachi, M. Sakairi, R.O. Suzuki, Aluminum bulk micromachining through an anodic oxide mask by electrochemical etching in an acetic acid/perchloric acid solution, Microelectron. Eng. 111 (2013) 14–20, https://doi.org/10.1016/j.mee.2013.05.007.
[24] K. Zhai, L. Du, Y. Wen, S. Wang, Q. Cao, X. Zhang, J. Liu, Fabrication of micro pits based on megasonic assisted through-mask electrochemical micromachining, Ultrasonics 100 (2020) 105990.
[25] Y. Sun, S. Ling, D. Zhao, J. Liu, Z. Liu, J. Song, Through-mask electrochemical micromachining of micro pillar arrays on aluminum, Surf. Coat. Technol. 401 (2020) 126277, https://doi.org/10.1016/j.surfcoat.2020.126277.
[26] J. Sun, W. Cheng, J.-L. Song, Y. Lu, Y.-K. Sun, L. Huang, X. Liu, Z.-J. Jin, C. J. Carmalt, I.P. Parkin, Fabrication of superhydrophobic micro post array on aluminum substrates using mask electrochemical machining, Chin. J. Mech. Eng. 31 (2018) 72, https://doi.org/10.1186/s10033-018-0270-1.
[27] G. Chen, M. Gao, R. Wei, Microconstituent-induced pitting corrosion in aluminum alloy 2024-T3, Corrosion 52 (1996).
[28] Z. Huda, N.I. Taib, T. Zaharinie, Characterization of 2024-T3: an aerospace aluminum alloy, Mater. Chem. Phys. 113 (2009) 515–517, https://doi.org/10.1016/j.matchemphys.2008.09.050.
[29] A. Merati, A study of nucleation and fatigue behavior of an aerospace aluminum alloy 2024-T3, Int. J. Fatigue 27 (2005) 33–44.
[30] M. Shao, Y. Fu, R. Hu, C. Lin, A study on pitting corrosion of aluminum alloy 2024-T3 by scanning microreference electrode technique, Mater. Sci. Eng. A 344 (2003) 323–327.
[31] M. Vukmirovic, N. Dimitrov, K. Sieradzki, Dealloying and corrosion of Al alloy 2024 T 3, J. Electrochem. Soc. 149 (2002) B428.
[32] L. Cacciatori, C. Brignoli, B. Mele, F. Gattere, C. Monti, M. Quadrio, Drag reduction by riblets on a commercial UAV, Appl. Sci. 12 (2022) 5070, https://doi.org/10.3390/app12105070.
[33] B. Mele, R. Tognaccini, P. Catalano, Performance assessment of a transonic wing–body configuration with riblets installed, J. Aircr. (2015), https://doi.org/10.2514/1.C033220.
[34] R. Garcia-Mayoral, J. Jiménez, Hydrodynamic stability and breakdown of the viscous regime over riblets, J. Fluid Mech. 678 (2011) 317–347.
[35] J. DeRose, A. Bałkowiec, J. Michalski, T. Suter, K. Kurzydlowski, P. Schmutz, Microscopic and Macroscopic Characterisation of an Aerospace Aluminium Alloy (AA2024), Witpress, 2012.
[36] F.M. Queiroz, M. Magnani, I. Costa, H.G. de Melo, Investigation of the corrosion behaviour of AA 2024-T3 in low concentrated chloride media, Corros. Sci. 50 (2008) 2646–2657, https://doi.org/10.1016/j.corsci.2008.06.041.
[37] T. Stimpfling, F. Leroux, H. Hintze-Bruening, Unraveling EDTA corrosion inhibition when interleaved into layered double hydroxide epoxy filler system coated onto aluminum AA 2024, Appl. Clay Sci. 83–84 (2013) 32–41, https://doi.org/10.1016/j.clay.2013.08.005.
[38] Z. Vargová, M. Almáši, L. Arabuli, K. Györyová, V. Zeleňák, J. Kuchár, Utilization of IR spectral detailed analysis for coordination mode determination in novel Zn-cyclen-aminoacid complexes, Spectrochim. Acta A Mol. Biomol. Spectrosc. 78 (2011) 788–793, https://doi.org/10.1016/j.saa.2010.12.022.
[39] X. Han, D. Zhang, Study on the micro-replication of shark skin, Sci. China Ser. E-Technol. Sci. 51 (2008) 890–896, https://doi.org/10.1007/s11431-008-0080-2.
[40] V. Moutarlier, R. Viennet, M.P. Gigandet, J.Y. Hihn, Use of ultrasound irradiation during acid etching of the 2024 aluminum alloy: effect on corrosion resistance after anodization, Ultrason. Sonochem. 64 (2020) 104879, https://doi.org/10.1016/j.ultsonch.2019.104879.
[41] P. Sun, Y. Wang, P. Liu, Y. Zhu, Y. Zhao, D. Zhao, H. Deng, Synergetic effect of 1, 2, 4-triazole and glycine on chemical mechanical planarization of aluminum at low polishing pressure in an eco-friendly slurry, ECS J. Solid State Sci. Technol. 9 (2020) 034003.
[42] Z. Wang, M. Sun, X. Niu, Y. Cui, J. Zhou, F. Meng, W. Zhou, Effect of glycine and TT-LYK in alkaline CMP slurry on controlling the galvanic corrosion at Al-Co interface, ECS J. Solid State Sci. Technol. 8 (2019) P496, https://doi.org/10.1149/2.0151909jss.
[43] Z. Wang, M. Sun, X. Niu, J. Zhou, Y. Cui, Effect of pH value and glycine in alkaline CMP slurry on the corrosion of aluminum by electrochemical analysis, ECS J. Solid State Sci. Technol. 8 (2019) P332, https://doi.org/10.1149/2.0221906jss.